Demonstration of a Novel Surface Plasmon Based Interferometer with COMSOL

Dominic Carrier and Jan J. Dubowski

Department of Electrical and Computer Engineering, Université de Sherbrooke

Sherbrooke, Québec, J1K 2R1, Canada, E-mail: dominic.carrier@usherbrooke.ca

Abstract: A novel method was developed to increase sensitivity of classical surface plasmon resonance (SPR) setup. This method consists in integrating to the SPR structure a self-referenced surface plasmon interferometer, where a change of refractive index will induce a shift of the resonance point but will also modulate the output response due to the optical path length difference of the SP modes in the interferometer structures. We conceptually demonstrate this integrated SP interferometer and its properties with the help of COMSOL Multiphysics®, a finite element method (FEM) simulation commercial software. We also highlight how the multiplexing of SP resonance signal to the interferometer modulation allows for greater accuracy of measurement.

Keywords: Interferometry, Surface Plasmons, SPR, FEM, COMSOL

1. Introduction

Surface plasmon resonance (SPR) is a well-known and well-established method, used in the contexts of label-free solutions characterization and biomolecular sensing ([1], chap. 1). SPR has been commercially available for nearly 20 years [2] and although it gained considerable popularity [3-6] and the related technology evolved, there is yet to be a major breakthrough made to allow mass-applicaton of this technology by the end-users. Some biosensing platforms provides avenues to address this accessibility issue, either by miniaturization of the classical SPR setups [[7, 8]], or by integrating directly the underlying concepts of SPR within a monolithically fabricated architecture [9].

In order to push further the sensitivity of SPR, advanced optical setups are often proposed in the literature [10-12]. Unfortunately, those extensive setups work against the effort to increase accessibility to the SPR biosensors. The integration of such a setup may provide a solution to this concern. As an example, integrated interferometers were already demonstrated for surface plasmons (SP) [13]. Along this trend, the proposed method in this document aims at increasing the sensitivity of SPR while still allowing usage of an integrated architecture. This integrated interferometer has the advantage of being uni-dimensional, well-suited to micro-fabrication techniques and inherently compatible with the SPR measurement, which is the most important point. The integrated SP based interferometer is merged directly with the SPR architecture.

Conceptually, an incident beam is coupled to SP modes using finite gratings. Those coherent SPs will propagate at the metal-dielectric interface and interfere together. The resulting interference is dependent on the optical path length difference of the two SPs, perfectly akin to a classical interferometer. The following figure (fig. 1) illustrates this conceptual setup.
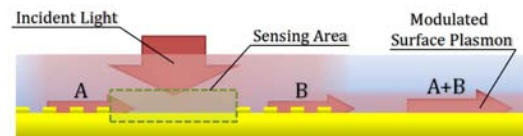

Figure 1 - Conceptual integrated interferometer setup. The finite gratings couple the incident light into SP modes with distinct optical paths. The sensing area denoted on the image is the region were one mode (A) will be phase-retarded in relation to the other (B), thus inducing interference when both modes are superposed again (A+B).

To demonstrate this, we used COMSOL Multiphysics' FEM simulations and obtained verification of the optical properties of this microstructure, its spectral characteristics and its behaviour under refractive index change, thus emulating the surface exposure to biological pathogens.

2. Methodology

The simulations were produced with incremental complexity, starting with the observation of the spectral response of a classical semi-infinite metal-dielectric interface with an infinite grating. By definition, the spectral response is the coupling efficiency of the incident energy to the SP mode via the first order of diffraction of the grating [14], for specific incident angles and energies (see figure 2-A for the model architecture). The architecture consists of two subdomains, the top one representing the dielectric milieu and the bottom one, the metal substrate. The top subdomain is bordered by a perfectly matched layer (PML), in order to absorb the scattered waves. The top boundary is set to a scattering boundary condition (SBC), with its source field being the incident field described below (eq. {1} or {2}). Formally, the incident wave equation will be expressed as follow at the incident boundary (with dielectric refractive index of n_j):

$$\Psi(\theta, E) = E_0 e^{-iEt/\hbar} e^{ik_y \cdot y} \cdot e^{ik_x \cdot x} \qquad \{1\}$$

$$\Psi_{\text{dual}}(\theta, E) = \Psi(\theta, E) \cdot \frac{(1 + e^{-2ik_x \cdot x})}{2} \quad \{2\}$$

Where
$$k_x = k_j \cdot \sin(\theta)$$
$$k_y = k_j \cdot \cos(\theta)$$
$$k_j = n_j \cdot \frac{E}{c_0 \hbar}$$

To emulate the lateral infinite expansion of the simulation domain, the side boundaries are configured as periodic boundaries in relation to the grating. In order to have a valid definition of the incident and scattered fields, only specific incident angles are considered viable for any energy (to respect the periodic condition). The acceptable angle must therefore fulfill the following condition:

$$\theta = \text{asin}\left(m \cdot \frac{k_L}{k_j}\right) = \text{asin}\left(\frac{m}{L} \cdot \frac{\pi \hbar c_0}{n_j E}\right) \quad \{3\}$$
Where $m \in \mathbb{N}_0$ and $mk_L \leq k_j$

To alleviate this restriction, equation {2} represents a dual-incidence electromagnetic (EM) plane wave, allowing twice as much

acceptable angle compared to the single-incidence EM wave (using $2k_j$ instead of k_j in equation {3}). It also allows usage of symmetry axes boundary conditions instead of periodic boundary conditions, which will prove to be more practical in the other simulations. Finally, the bottom boundary is set as a perfect electric conductor (PEC, acting as a perfectly reflecting boundary), though the thickness of the metal substrate is largely sufficient to reflect all the incident energy. Refractive indexes of Au and air used in the simulations for 1.305 eV (950 nm) were obtained from the literature [15, 16]. The simulations were realised with COMSOL RF module's "In-Plane TM wave" application mode, with the "Scattered wave" formulation.
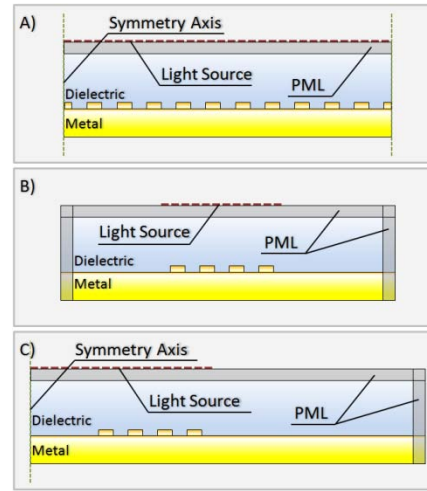

Figure 2 - Simulation architectures (not to scale). Results were produced at normal incidence, sweeping in incident energy. A) Infinite grating architecture; the light source is described by equations {2}. B) Finite grating architecture. C) Cavity / integrated interferometer architecture.

The second simulation is derived from the same template, but replaces the infinite grating at the interface by a finite one. As the grating is now finite, the lateral infinite expansion of the simulation domain is no longer required; therefore, the side boundaries are replaced with PML (see fig 2-B). This second simulation is used to observe the effect of a finite grating on the diffraction capability of the microstructure and the resulting modification of its spectral response.

The final simulation is the observation of two adjacent finite grating separated by a specific

distance (the cavity length). Based on the previous model architecture (fig 2-B), the left PML is replaced by a PEC to emulate a symmetry axis in the middle of the cavity between the two finite gratings (see fig 2-C). This simulation model will highlight the interference fringes created within the envelope of the finite gratings diffraction spectral response. Afterwards, we will demonstrate the usage of that microstructure in the context of biosensing.

3. Results

Due to the angle restriction of the lateral infinite extension of the simulation model, it is more interesting and convenient to observe the spectral response of the system in the energy domain instead of the angular domain; using a normal incidence, a direct comparison of spectral responses at any energy can be made with similar resolution, for all simulations.

3.1 Microstructures' spectral response

The first part of the results presents the characteristic spectral responses of different architectures, illustrated by the following relations for the spectral responses in reflection. Conceptually, the spectral response is the amount of energy not reflected back, due to diffraction into SP modes; it can be qualified as the transmission spectral response. As it is not directly observable experimentally, it is preferable to have a second definition for the spectral response expressed by the reflection; it is illustrated by the following equation (eq. {4}), where $\mathbb{S}_R$ and $\mathbb{S}_T$ stand for the spectral response in reflection and transmission, respectively.

$$\mathbb{S}_R = \frac{I_R}{I_{Total}}$$
$$\mathbb{S}_T = \frac{I_{SP}}{I_{Total}} \approx 1 - \mathbb{S}_R \qquad \{4\}$$

The relative estimator used here to represent the reflection spectral response is the **net relative power flow** along the interface's **normal** (projection of the Poynting vector on the normal), averaged for the top boundary. This estimator is valid for either single- or dual-incidence, and for any incident angle and energy, as long as the intensity of unwanted scattering is low in relation to the intensity diffracted in surface plasmon modes. For the transmission spectral response, the relative estimator used is again the net relative power flow but this time along the interface itself, within the metal substrate. As there is no net power flow along the interface in case of dual incidence, an equivalent relative estimator is used: the intensity of the scattered fields within the metal domain (the averaged electromagnetic energy density).

The following image (figure 3-A) illustrates the spectral responses (in energy) of the three architectures. We first observe the characteristically narrow and intense resonance peak of the infinite grating structure. When the
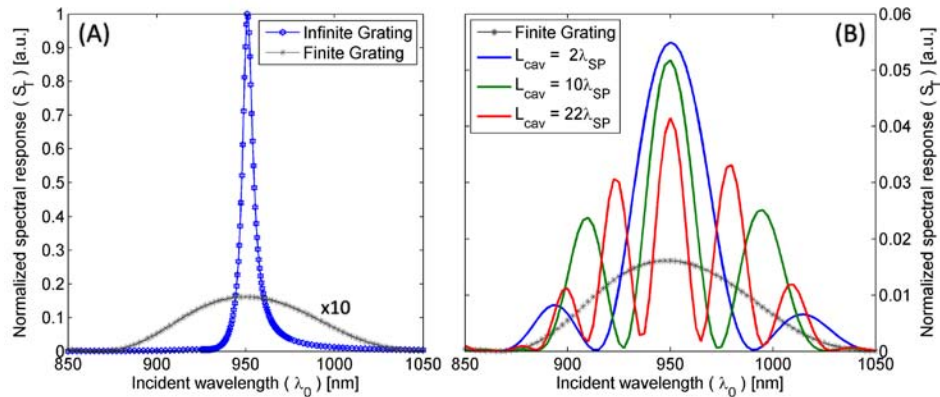

Figure 3 - Spectral responses of the three simulated architectures (equation {4} for $\mathbb{S}_T$ definition and figure 2 for architectures). A) Comparison between resonance shape of an infinite grating and finite grating (x10). B) Spectral responses of the integrated interferometer, for different cavity lengths. The finite grating curve is also associable to an "infinite length" cavity.

grating is finite, this peak broadens and secondary lobes are observed further away from resonance (not illustrated here). The observed shape is characteristic of a sinus cardinal, for lengths of grating of the order of the SP propagation length or smaller. The addition of a second finite grating adjacent to the first one will produce interference of the SP modes, thus causing the interference fringes modulated by the diffraction envelope.

Two behaviours are worth mentioning in the spectral responses. The length of the finite grating(s) affects the width of the main lobe: the smaller the grating, the wider the *sinc* main lobe will be. The second interesting behaviour is related to the cavity length. As the cavity length is increased, the interference fringes will get smaller and narrower, as illustrated in figure 3-B. When the length goes toward infinity, the fringes will disappear, leaving only the single grating spectral response. The diminution of the interference effect with the distance is directly related to the exponential decay of the SPs as they propagate.

3.2 Biosensing application

Let's now observe those spectral responses and their alteration under a change of refractive index, confined near the metal-dielectric interface. In this case, the change of refractive index emulates the specific chemical adsorption of biomolecules at the surface of the biosensor. A thin layer of material is added on top of the

metal-dielectric interface (125nm thick) which adds to the background dielectric refractive index a positive Δn refractive index difference. As this difference increases, it emulates the increase in concentration.

The image below (figure 4) presents the infinite grating and the integrated interferometer spectral responses under a change of the refractive index. As expected, such a change induces a shift of the resonance energy in both cases. The important point to assess here is that the different microstructure on top of the thin layer has no direct effect on the SP resonance. As observed on the image (see figure 4), both the peak (left) and the envelope (right) inherently present the same shifts for equivalent refractive index differences. Within the envelope (right), we can clearly observe the interference fringes induced by the combination of the two gratings, also shifting by the same equivalent amount. This equal shift is caused by the inherent dependence of the optical path length to the propagation of surface plasmons on the interface [17].

The experimental detection of the surface plasmon resonance requires the tracking of a single resonance peak as it shifts either in angle or energy (incident wavelength). By adding a microstructure on top of the classical SPR architecture, it is possible to customize the microstructure's diffraction pattern and multiplex that spectral response to the SP resonance.
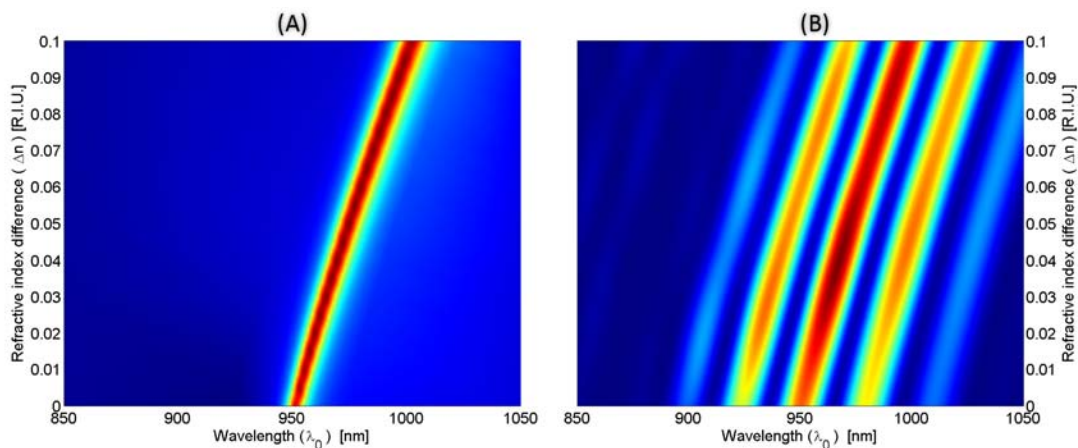
The diffraction pattern caused by the

Figure 4 - Spectral responses' shift under a change of refractive index. A) Infinite grating architecture. B) Integrated interferometer architecture, for cavity length equivalent to half the SP mode propagation length ($27\lambda_{SP}$). We note the envelope on the right associable to that of the finite gratings' diffraction.

interferometer setup induces a modification of the SPR signal, broadening its envelope and adding sub-features (interference fringes). As those features are entirely predictable and fixed for a specific topping microstructure, this multiplexed signal can be used to increase shift measurement precision by using fitting algorithm and advanced statistical correlation methods, thus leading to increased sensitivity.

3.3 Far-field measurability

As mentioned earlier, the previously presented spectral response represents the energy transfer from the incident wave to the SP mode (see $\mathbb{S}_T$ in equation {4}). Experimentally speaking, the intensity of the SP mode cannot be measured easily or conveniently. The microstructure was designed to provide an accessible measurement method that would reflect the interferometer's response on the system.

The next figure (fig. 5) presents the spectral response in reflection ($\mathbb{S}_R$) for the integrated interferometer (setup reference at fig. 2-C), calculated using the estimator described in section 3.1. It is possible to observe right away the interference fringes and the diffraction envelope.
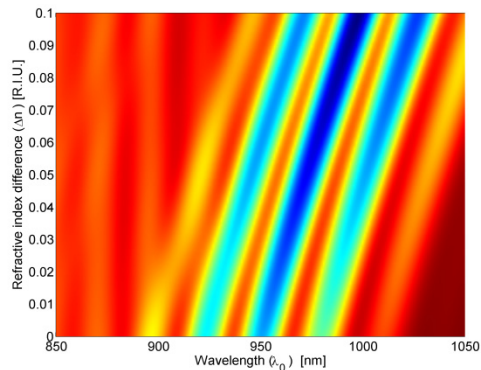

Figure 5 - Far-field spectral response ($\mathbb{S}_R$) of the integrated SP interferometer setup. It can be directly compared against figure 4-B. Observable features on the left of the envelope (e.g. vertical lines around 870nm and 895nm) are consequences of non-confined diffraction and are unrelated to SP modes.

This equivalence is explained by the fact that when the energy is not coupled to the surface plasmon mode (due to destructive interference), it will be strongly reflected back where it came from, and conversely. Thus, the energy flow observed in the near-field ($\mathbb{S}_T$) will be projected to the far-field ($\mathbb{S}_R$).

4. Conclusions

Through this paper, COMSOL Multiphysics was successfully used to illustrate the effect of microstructures on the top of a classical SP setup metal-dielectric interface. The results obtained with our simulations are consistent with the widely known and accepted theory of SP diffraction, stated by the eponymous 1988 booklet written by Raether [14]. As those simulations are pushed further to observe the effect of complex microstructures, the near-field interference of the diffracted SP mode was investigated. Observations were made of the diffraction envelope being modulated by the interference effect caused by the interaction of the two diffracted SP modes. The displacement of the envelope and the interference fringes were also characterized under a refractive index change. Finally, it was highlighted that those additional signal features can be used to increase the tracking precision of the SPR shift, therefore accounting for the claimed increase in the conceptual measurement sensitivity.

5. Acknowledgements

6. References

1. *Label-Free Biosensors - Techniques and Applications*, ed. M.A. Cooper. 2009: Cambridge University Press. 300.
2. *http://www.biacore.com/lifesciences/history /index.html*
3. Homola, J., S.S. Yee, and G. Gauglitz, *Surface plasmon resonance sensors: review.* Sensors and Actuators B: Chemical, 1999. **54**(1-2): p. 3-15.
4. Rich, R.L. and D.G. Myszka, *Survey of the year 2006 commercial optical biosensor*

literature. Journal of Molecular Recognition, 2007. **20**(5): p. 300-366.

5. Rich, R.L. and D.G. Myszka, *Survey of the year 2007 commercial optical biosensor literature.* Journal of Molecular Recognition, 2008. **21**(6): p. 355-400.

6. Rich, R.L. and D.G. Myszka, *Grading the commercial optical biosensor literature— Class of 2008: 'The Mighty Binders'.* Journal of Molecular Recognition, 2010. **23**(1): p. 1-64.

7. *Spreeta™ Technology http://www.sensata.com /sensors/spreeta-analytical-sensor-highlights.htm*

8. Chinowsky, T.M., et al., *Performance of the Spreeta 2000 integrated surface plasmon resonance affinity sensor.* Sensors and Actuators B: Chemical, 2003. **91**(1-3): p. 266-274.

9. Lepage, D. and J.J. Dubowski, *Surface plasmon effects induced by uncollimated emission of semiconductor microstructures.* Opt. Express, 2009. **17**(12): p. 10411-10418.

10. Lee, J.-Y., T.-K. Chou, and H.-C. Shih, *Polarization-interferometric surface-plasmon-resonance imaging system.* Opt. Lett., 2008. **33**(5): p. 434-436.

11. Patskovsky, S., et al., *Mechanical modulation method for ultrasensitivephase measurements in photonicsbiosensing.* Opt. Express, 2008. **16**(26): p. 21305-21314.

12. Patskovsky, S., et al., *Self-noise-filtering phase-sensitive surface plasmon resonance biosensing.* Opt. Express, 2010. **18**(14): p. 14353-14358.

13. Bozhevolnyi, S.I., et al., *Channel plasmon subwavelength waveguide components including interferometers and ring resonators.* Nature, 2006. **440**(7083): p. 508-511.

14. Raether, H., *Surface Plasmons on Smooth and Rough Surfaces and on Gratings (Springer Tracts in Modern Physics).* 1988: Springer.

15. Thèye, M.-L., *Investigation of the Optical Properties of Au by Means of Thin Semitransparent Films.* Physical Review B, 1970. **2**(8): p. 3060.

16. Palik, E.D., *Handbook of optical constants of solids.* 1985, Orlando: Academic Press.

17. Carrier, D., *Interférométrie auto-référencée par plasmons de surface - Une approche vers la biodétection*, in *Département de génie électrique*. 2010, Université de Sherbrooke: Sherbrooke. p. 96.